Superlattice structure in the antiferromagnetically ordered state in the Hubbard model on the Ammann-Beenker tiling

Akihisa Koga◉

Department of Physics, Tokyo Institute of Technology, Meguro, Tokyo 152- 8551, Japan

We study magnetic properties in the half-filled Hubbard model on the Ammann-Beenker tiling. First, we focus on the domain structure with locally eightfold rotational symmetry to examine the strictly localized confined states for the tight-binding model. We count the number of vertices and confined states in the larger domains generated by the deflation operations systematically. Then, the fraction of the confined states, which plays an important role for magnetic properties in the weak coupling limit, is obtained as $p = 1/2\tau^2$, where $\tau(=1 + \sqrt{2})$ is the silver ratio. It is also found that the wave functions for confined states are densely distributed in the system and thereby the introduction of the Coulomb interactions immediately induces the finite staggered magnetizations. Increasing the Coulomb interactions, the spatial distribution of the magnetizations continuously changes to those of the Heisenberg model. We discuss crossover behavior in the perpendicular space representation and reveal the superlattice structure in the spatial distribution of the staggered magnetizations.

I. INTRODUCTION

Quasicrystal without translational symmetry has attracted much interest since its first observation in the Al-Mn array [1]. Among them, the Au-Al-Yb array with Tsai-type clusters [2] is one of the interesting examples with anomalous low temperature properties. The quasicrystal $Au_{51}Al_{34}Yb_{15}$ shows quantum critical behavior with unusual exponents, while the approximant $Au_{51}Al_{35}Yb_{14}$ shows heavy fermion behavior [3]. These experiments should clarify that electron correlations play an important role in the quasicrystals. Furthermore, the superconductivity has recently been observed in the Al-Zn-Mn quasicrystal [4], stimulating further investigations on electron correlations and induced ordered states in the quasiperiodic systems [5–14].

Up to now, no magnetically ordered states have been found in the quasicrystals although it has recently been observed in the approximants Cd_6Tb [15], Au-Al-Gd [16], and Au-Al-Tb [17]. In contrast to the experiments, there are many theoretical works for the spontaneously symmetry breaking states on the two-dimensional quasiperiodic lattices. Among them, the system on the Penrose tiling [18–24] has been examined, where the magnetically ordered states [12,25–29], superconductivity [11,13,14], and excitonic insulator [30] have been discussed. The Ammann-Beenker tiling [31,32] (see Fig. 1) is another example for two-dimensional quasiperiodic structures, where the superconducting [33] and higher order topological states [34] have recently been examined. The magnetic instability has been discussed in the Hubbard [35], Heisenberg [36,37], and Anderson lattice [38] models. However, the system size treated is not large enough to discuss magnetic properties inherent in the quasiperiodic lattice. In particular, the role of the strictly localized states, which should play a crucial role in the weak coupling limit, has not been discussed up to now. Therefore, it is instructive to examine the confined states

and to clarify magnetic properties in the Hubbard model with larger clusters.

In the paper, we study the half-filled Hubbard model on the Ammann-Beenker tiling. First, we focus on the macroscopically degenerate states in the noninteracting case. By examining the domain structures generated by the deflation operations systematically, we obtain the fraction of the confined states in the thermodynamic limit. To clarify the effects of the Coulomb interactions, we apply the real-space Hartree approximation to the system and calculate the local magnetization at each site. We reveal that the superlattice structure appears in the weak coupling case. Mapping the spatial distribution of the magnetization to the perpendicular space, we also discuss the crossover in the antiferromagnetically ordered state.

The paper is organized as follows. In Sec. II, we introduce the half-filled Hubbard model on the Ammann-Beenker tiling. In Sec. III, we study the confined states with $E = 0$, which should play an important role for magnetic properties in the weak coupling limit. Counting the number of the confined states in the domains systematically, we exactly obtain their fraction. We discuss how the antiferromagnetically ordered state is realized in the Hubbard model in Sec. IV. The crossover behavior in the ordered state is addressed, by mapping the spatial distribution of the magnetization to the perpendicular space. A summary is given in the last section.

II. MODEL AND HAMILTONIAN

We study the Hubbard model on the Ammann-Beenker tiling, which should be given by the following Hamiltonian,

$$H = -t \sum_{\langle ij \rangle \sigma} (c_{i\sigma}^{\dagger} c_{j\sigma} + \text{H.c.}) + \sum_i U \left(n_{i\uparrow} - \frac{1}{2} \right) \left(n_{i\downarrow} - \frac{1}{2} \right),$$
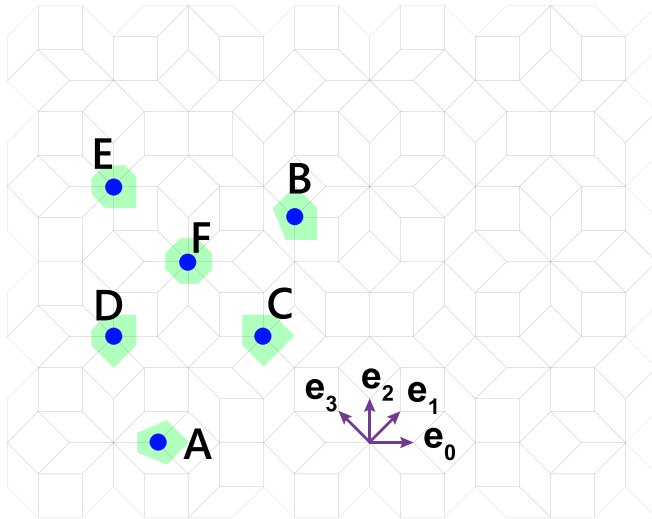
(1)

FIG. 1. Ammann-Beenker tiling and six types of vertices. The shaded regions represent the corresponding Voronoi cells. $\mathbf{e}_0, \mathbf{e}_1, \mathbf{e}_2$, and $\mathbf{e}_3$ are projection of the fundamental translation vectors in four dimensions, $\mathbf{n} = (1, 0, 0, 0), (0, 1, 0, 0), (0, 0, 1, 0),$ and $(0,0,0,1)$.

where $c_{i\sigma} (c_{i\sigma}^\dagger)$ annihilates (creates) an electron with spin $\sigma(=\uparrow, \downarrow)$ at the ith site and $n_{i\sigma} = c_{i\sigma}^\dagger c_{i\sigma}$. t is the transfer integral and U is the onsite Coulomb interaction. Since the Hubbard model on the Ammann-Beenker tiling is bipartite, the chemical potential is always $\mu = 0$ when the electron density is fixed to be half filling.

The Ammann-Beenker tiling is composed of squares and rhombuses, which is schematically shown in Fig. 1. There exist six types of vertices. In the paper, the vertices are denoted as A, B, ..., and F for the coordination number 3, 4, ..., and 8, respectively. Since the vertex lattice is bipartite, it is naively expected that the introduction of the Coulomb interactions induces the magnetically ordered state with the staggered moments. According to the Lieb's theorem [39], the half-filled Hubbard model on the bipartite lattice has the total spin $S_{\text{tot}} = \frac{1}{2}|N_A - N_B|$ in the ground state, where N_A and N_B are the numbers of sites in the A and B sublattices. Therefore, the imbalance in their numbers yields the ferrimagnetically ordered state, e.g., Lieb lattice [40]. In our model, one can prove that the antiferromagnetically ordered state is realized without uniform magnetizations, considering the deflation rule. Figure 2 shows the deflation rule for the directed squares and rhombuses, where the open and solid circles at the corners represent the distinct sublattices. By applying the deflation operations to the squares and rhombuses, their numbers are changed as

$$\begin{pmatrix} S_\uparrow^{n+1} \\ S_\downarrow^{n+1} \\ R_\uparrow^{n+1} \\ R_\downarrow^{n+1} \end{pmatrix} = \begin{pmatrix} 1 & 2 & 2 & 2 \\ 2 & 1 & 2 & 2 \\ 0 & 2 & 2 & 1 \\ 2 & 0 & 1 & 2 \end{pmatrix} \begin{pmatrix} S_\uparrow^n \\ S_\downarrow^n \\ R_\uparrow^n \\ R_\downarrow^n \end{pmatrix}, \quad (2)$$

where $S_\sigma^n (R_\sigma^n)$ is the number of squares (rhombuses) with spin σ at iteration n, whose spin is defined by spins connected by the arrows in Fig. 2. It is known that in the thermodynamic limit ($n \to \infty$), the numbers of squares and rhombuses τ^2 times increase for each deflation process and $S/R = 1/\sqrt{2}$,
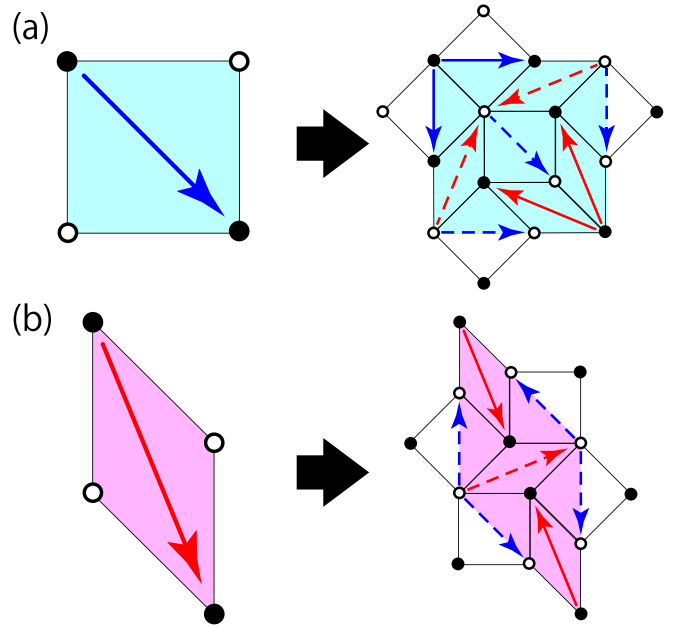

FIG. 2. Deflation rule for directed square (a) and rhombus (b) in the Ammann-Beenker tiling. Solid (dashed) arrows represent the directed squares and rhombuses with spin σ ($\bar{\sigma}$). Open and solid circles at the corners represent the distinct sublattices.

where $S = \sum_\sigma S_\sigma, R = \sum_\sigma R_\sigma$, and $\tau(=1 + \sqrt{2})$ is the silver ratio [31,32]. From the above relation Eq. (2), we obtain that $S_\sigma = S/2$ and $R_\sigma = R/2$ in the thermodynamic limit. Since the number of squares and rhombuses are independent of spins in the thermodynamic limit, the vertices are also independent. Its proof is explicitly shown in Appendix A. Then, we can say that the antiferromagnetically ordered state without uniform magnetizations is realized in the thermodynamic limit.

On the other hand, the magnetization profile may not be trivial since in the quasicrystals, each lattice site is not equivalent, in contrast to the conventional lattice with translational symmetry. In particular, in the weak coupling limit, magnetic properties strongly depend on the noninteracting density of states (DOS) at the Fermi level. Figure 3 shows the DOS in the tight-binding model on the Ammann-Beenker tiling [33].
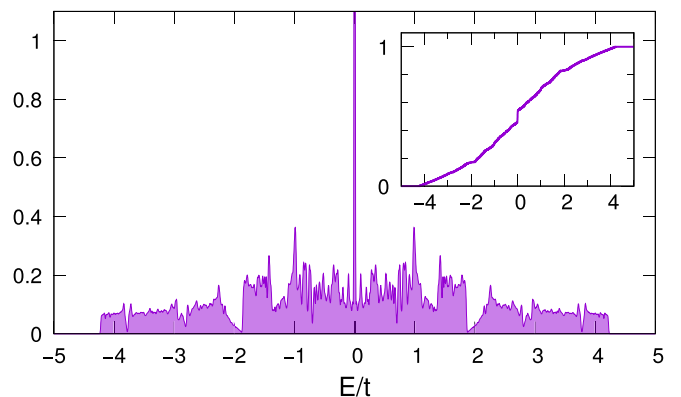

FIG. 3. Density of states in the tight-binding model on the Ammann-Beenker tiling with $N = 1\,049\,137$. The inset shows the integrated density of states.
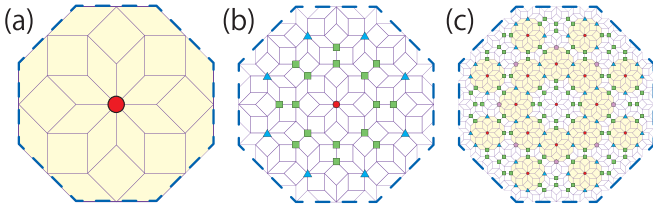
FIG. 4. (a), (b), and (c) are the domains D_1, D_2, and D_3, respectively. Solid triangles, squares, pentagons, and circles represent C, D, E, and F vertices. Shaded regions represent the D_1 domains. For clarification, the lattice constants are not rescaled (see Fig. 2).

We find the delta-function-like peak at $E = 0$, meaning the existence of the confined states. When magnetic properties are studied at half filling, the confined states should play an essential role in understanding magnetic properties. In the following section, we focus on these macroscopically degenerate states with $E = 0$.

III. CONFINED STATES IN THE TIGHT-BINDING MODEL ON THE AMMANN-BEENKER TILING

In the section, we focus on the confined states in the tight-binding model. As seen in Fig. 3, the eigenstates are macroscopically degenerate at $E = 0$, which means that the corresponding states are exactly localized in certain regions. This is similar to the model on the Penrose tiling [12,18,23]. The key of the confined states is the fact that the Ammann-Beenker tiling has the eightfold rotational symmetry. Here, we focus on the F vertex with locally eightfold rotational symmetry, which is closely related to the confined states, as discussed later. Due to the matching rule of the Ammann-Beenker tiling, there always appear eight squares and sixteen rhombuses around each F vertex, as shown in Fig. 4(a). For convenience, when the local eightfold rotational symmetry is satisfied in the domain shown in Fig. 4(a) and is not satisfied outside, we define this domain composed of seventeen sites (the boundary sites are excluded) as D_1. By applying the deflation operation to the domain D_1, a new domain is generated, as shown in Fig. 4(b). If one focuses on the F vertex at the center, the rotational symmetry is satisfied in the domain with larger

lattice sites, which is bounded by the regular octagon shown as the dashed line in Fig. 4(b). This domain is denoted as D_2. Repeating the deflation operations, we obtain the D_i domains. Then, we can define the F vertex at the center of the domain D_i as F_i. Figure 4 shows the domains D_1, D_2, and D_3, where F_1, F_2, and F_3 vertices are located at their centers, respectively. In the D_3 domain, we find sixteen D_1 domains with the F_1 vertices. We wish to note that there does not exist the D_1 domain at the center because of its definition. This allows us to uniquely determine F_i as the center site of the domain D_i. It is known that, in each deflation operation, F_i ($i > 1$) vertices are generated from the F_{i-1} vertices and the F_1 vertices are generated from half of the C vertices, and D and E vertices (see Fig. 4). Then, in the thermodynamic limit, the fraction of the F_i vertices is obtained as

$$p^{F_i} = 2\tau^{-(2i+3)}, \tag{3}$$

since $p^{F_1} = (\frac{1}{2}p^C + p^D + p^E)/\tau^2 = 2\tau^{-5}$ and $p^{F_{i+1}} = p^{F_i}/\tau^2$, where p^α is the fraction of the $\alpha (=$A, B, C, D, E, and F) vertex [32]: $p^A = \tau^{-1}$, $p^B = 2\tau^{-2}$, $p^C = 2\tau^{-3}$, $p^D = 2\tau^{-4}$, $p^E = \tau^{-5}$, $p^F = \tau^{-4}$. Since the F_i vertex is defined as the center vertex of the domain D_i, the fraction of the domain D_i is given as $p_i = p^{F_i}$.

By counting the numbers of all vertices up to the domain D_{11} numerically, we obtain the domain profile, as shown in Table I. Its fraction $p_i^\alpha (= N_i^\alpha/N_i)$, where N_i^α is the number of α vertices and $N_i (= \sum_\alpha N_i^\alpha)$ is the number of sites in the domain D_i, is shown in Fig. 5. From these data, one finds relations between the number of vertices. For example, $N_{i+1}^C = 2N_i^A$, $N_{i+1}^D = N_i^B$, $N_{i+2}^E = N_i^A$, and $N_{i+1}^F = N_i^C/2 + N_i^D + N_i^E + N_i^F$. Estimating the general terms for N_i^A, N_i^B, and N_i as

$$N_i^A = 2\sqrt{2}[(-\tau)^{1-i} - \tau^{i-1}] + 4[\tau^{2i-1} - \tau^{1-2i}], \tag{4}$$

$$N_i^B = 8[\tau^{2i-2} + \tau^{2-2i} - \delta_{i1}], \tag{5}$$

$$N_i = 1 + 2\sqrt{2}[(-\tau)^{-i} - \tau^i] + 4[\tau^{2i} + \tau^{-2i}], \tag{6}$$

we obtain the general terms for all vertices in each domain. Namely, the domain D_∞ can be regarded as the Ammann-Beenker tiling in the thermodynamic limit and we have confirmed that the fraction for each vertex $p_\infty^\alpha =$

TABLE I. Profile of each domain D_i. p_i is its fraction, N_i is the number of vertices, and N_i^α is the number of α vertices in the ith domain, where the sites on the boundary are excluded. N_{i1} is the number of the D_1 domain structure in the ith domain. N_i^{tot} is the total number of the confined states and N_i^{net} is the net number of the confined states in the ith domain (see text).

| i	p_i	N_i	N_i^A	N_i^B	N_i^C	N_i^D	N_i^E	N_i^F	N_{i1}	N_i^{tot}	N_i^{net}
1	$2\tau^{-5}$	17	8	8	0	0	0	1	1	2	2
2	$2\tau^{-7}$	121	48	48	16	8	0	1	0	6	6
3	$2\tau^{-9}$	753	312	272	96	48	8	17	16	44	12
4	$2\tau^{-11}$	4 521	1 872	1 584	624	272	48	121	104	324	20
5	$2\tau^{-13}$	26 673	11 048	9 232	3 744	1 584	312	753	632	2 110	30
6	$2\tau^{-15}$	156 249	64 720	53 808	22 096	9 232	1 872	4 521	3 768	12 938	42
7	$2\tau^{-17}$	912 593	378 008	313 616	129 440	53 808	11 048	26 673	22 152	77 112	56
8	$2\tau^{-19}$	5 323 593	2 205 104	1 827 888	756 016	313 616	64 720	156 249	129 576			
9	$2\tau^{-21}$	31 039 313	12 856 904	10 653 712	4 410 208	1 827 888	378 008	912 593	756 344			
10	$2\tau^{-23}$	180 937 273	74 946 672	62 094 384	25 713 808	10 653 712	2 205 104	5 323 593	4 411 000			
11	$2\tau^{-25}$	1 054 644 657	436 848 120	361 912 592	149 893 344	62 094 384	12 856 904	31 039 313	25 715 720			
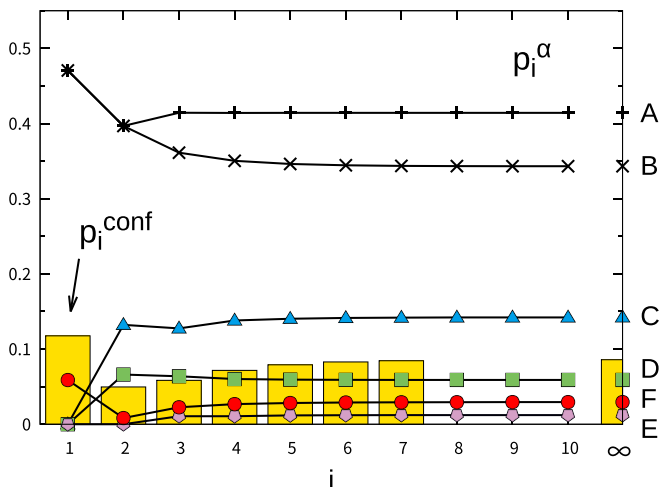
FIG. 5. Symbols represent the fractions of the α vertex p_i^α and bars represent the fraction of confined state $p_i^{\rm conf}$ in the ith domain. On the right edge of the figure, the corresponding fractions in the thermodynamic limit are shown (see text).

$\lim_{i\to\infty} N_i^\alpha/N_i$ is reduced to the well-known value p^α [32] (see Fig. 5).

Now, we consider the confined states in each domain with the eightfold rotational symmetry. In the domain D_1, there are two confined states. Since the confined states satisfy the Schrödinger equation $H\Psi = 0$ with $U = 0$, it is always possible to choose each eigenstate such that it can be described by the irreducible representation of the point group D_8. Table II shows a part of the irreducible characters of the dihedral group D_8, where there exist four one-dimensional irreducible representations. Namely, the confined states Ψ_1 and Ψ_2, which are schematically shown in Fig. 6, are described by the irreducible representation B_1 and B_2, and $\langle\Psi_1|\Psi_2\rangle = 0$. We wish to note that these confined states are always exact eigenstates even when the system does not have eightfold rotational symmetry outside of the domain D_1. We also find that the amplitudes of the wave function Ψ_1 are finite only in the sublattice B, and the others are in the sublattice A when the sublattice for the center site is regarded as the sublattice A. This is in contrast to the case in the vertex model on the Penrose tiling [18,23], where finite amplitudes appears in one of the sublattices in the *cluster* defined in Ref. [12]. This should induce distinct spatial distribution of the magnetization in the weak coupling limit, which will be discussed in the next section.

In the domain D_2, there is the structure of the domain D_1 around the center. Therefore, in the domain D_2, Ψ_1 and

TABLE II. A part of the irreducible characters of the dihedral group D_8. E is an identity operator, C_8 is a rotation operator of $\pi/4$, and I_y is a reflection operator about the y axis.

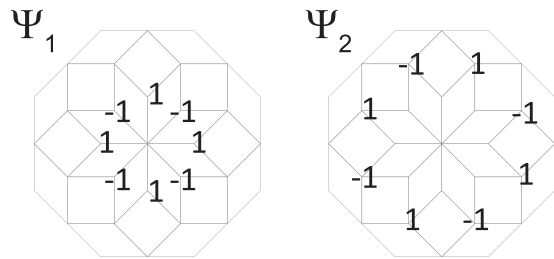|	E	C_8	I_y	$I_y C_8$
A_1	1	1	1	1
A_2	1	1	-1	-1
B_1	1	-1	1	-1
B_2	1	-1	-1	1

FIG. 6. Two confined states in the domain D_1 for the tight-binding model on the Ammann-Beenker tiling. The number at the vertices represent the amplitudes of the confined state.

Ψ_2 located there are the confined states. Furthermore, we find four confined states Ψ_3, Ψ_4, Ψ_5, and Ψ_6, as shown in Fig. 7. It is found that these confined states are described by the irreducible representations A_2, B_1, A_1, and B_2. Namely, Ψ_1 and Ψ_4 (Ψ_2 and Ψ_6) are described by the same irreducible representation B_1 (B_2), but there is no overlap in their wave functions [41]. In the domain D_3, in addition to the six confined states shown above, we find six confined states Ψ_7, Ψ_8, ..., and Ψ_{12}, which are explicitly shown in Fig. 8. These are described by the irreducible representations A_2, B_1, B_1, B_2, A_1, and B_2. We note that, in the domain D_3, there exist sixteen D_1 domains (shown as the shaded regions in Figs. 4 and 8), where two confined states Ψ_1 and Ψ_2 exist locally. Therefore, in the domain D_3, the net number of the confined states $N_3^{\rm net} = 12$, and the total number of the confined states $N_3^{\rm tot} = N_3^{\rm net} + 16N_1^{\rm net} = 44$, with $N_1^{\rm net} = 2$.

To count the number of the confined states in larger domains systematically, we perform the exact diagonalization method for the tight-binding Hamiltonian. Some details are discussed in Appendix B. The results up to the domain D_7 are shown in Table I. The net number of the confined states is evaluated by taking into account the smaller domain
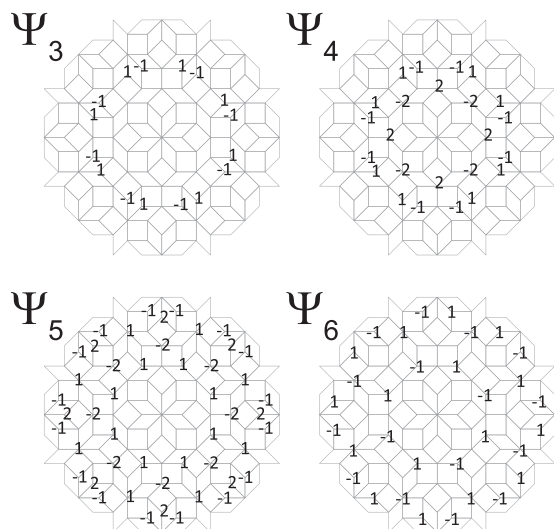

FIG. 7. Four confined states in the domain D_2 for the tight-binding model on the Ammann-Beenker tiling. The number at the vertices represents the amplitudes of confined state.
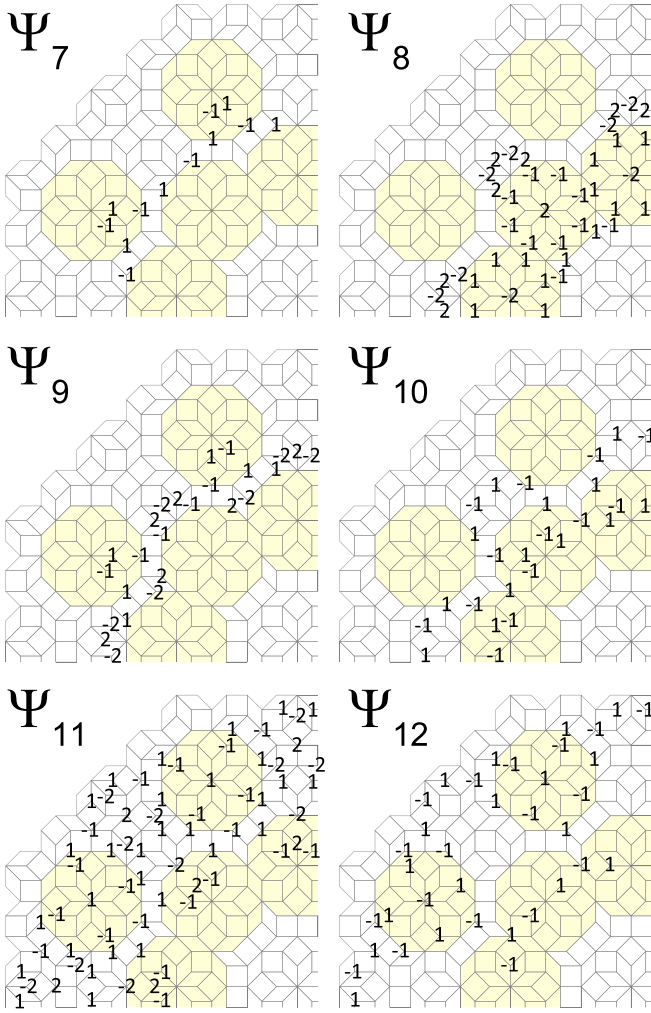
FIG. 8. Six confined states in the domain D_3 for the tight-binding model on the Ammann-Beenker tiling. For clarity, the quarter of the domain D_3 is shown. The shaded areas represent the D_1 domains inside of the domain D_3 and the F_1 vertex is located in each domain D_1. The number at the vertices represents the amplitudes of confined state.

structures, as

$$N_i^{\text{net}} = N_i^{\text{tot}} - \sum_{j=1}^{i-1} N_{ij} N_j^{\text{net}}. \quad (7)$$

Namely, N_{ij} satisfies the relations as $N_{i+1,j+1} = N_{ij}$, $N_{i1} = N_{i-1}^{\text{C}}/2 + N_{i-1}^{\text{D}} + N_{i-1}^{\text{E}}$, and $N_i^{\text{F}} = \sum N_{ij}$, where N_i^α is the number of the α vertex in the domain D_i. Since the net number of confined states should be given as $N_i^{\text{net}} = i(i+1)$, we obtain the fraction of the confined states in the tight-binding model on the Ammann-Beenker tiling as

$$p = \sum_i p_i N_i^{\text{net}} = \frac{1}{2\tau^2} \sim 8.579 \times 10^{-2}, \quad (8)$$

where p_i is the fraction of the D_i domain. We have also confirmed that it corresponds to the ratio in the domain D_∞,

$p = \lim_{i\to\infty} N_i^{\text{tot}}/N_i$, where the general term for the total number of the confined states is given as

$$\begin{aligned} N_i^{\text{tot}} = {} & 4 + 2\sqrt{2}[(-\tau)^{-i} - \tau^i] \\ & + 2(\tau^{2i-2} + \tau^{2-2i}) + i(i+1). \end{aligned} \quad (9)$$

In the following, we consider electron correlations in the Hubbard model to discuss how the antiferromagnetically ordered state is realized in the Ammann-Beenker tiling. In the weak coupling limit, it is, in principle, possible to evaluate the magnetization by means of the Gram-Schmidt orthogonalization for the confined states at $E = 0$ since their degeneracy should be lifted by the introduction of the Coulomb interactions. However, the confined states are densely distributed in the lattice. Figures 6–8 show that the confined states have amplitudes in almost the whole of the domain. In addition, the amplitudes of confined states in a certain domain D sometimes appear on the smaller domains inside of D, where some confined states exist locally. For example, in Fig. 8, the wave function Ψ_{11} has amplitudes in each domain D_1 (the shaded areas) with the local wave functions Ψ_1 and Ψ_2. Therefore, the wave functions for confined states multiply overlap in the space, which should induce fractal behavior in the magnetic pattern. This is in contrast to the Penrose-Hubbard model, where there exist a finite number of confined states in a certain region "*cluster*" and the seventy percents of magnetizations are exactly obtained in the thermodynamic limit [12]. Figure 9 shows the local magnetizations up to D_7 domain. When we focus on the D_1 domain, there are two confined states Ψ_1 and Ψ_2 which has finite amplitudes in eight sites for each. Therefore, there appears only the magnetization $m = 1/16$. In the larger domains, it is found that the distribution of the magnetization is classified into some groups. The group with large magnetizations is mainly contributed from the A and B vertices around the F vertex, which originates from the confined states Ψ_1 and Ψ_2 (see Fig. 6). In the paper, we apply the simple mean-field theory to the Hubbard model to discuss magnetic properties inherent in the Ammann-Beenker tiling [35].

IV. ANTIFERROMAGNETICALLY ORDERED STATE

In the section, we consider the Hubbard model with finite U. When the half-filled Hubbard model on the bipartite lattice is considered, the quantum Monte Carlo (QMC) method is one of the powerful methods to discuss ground-state properties. On the other hand, to discuss magnetic properties inherent in the quasiperiodic structure, the real-space Hartree approximation has an advantage in treating the large system size, which is crucial to clarify the superlattice structure in the magnetization pattern, as discussed later.

The mean-field Hamiltonian (1) is reduced to

$$H_{\text{MF}} = -t \sum_{\langle ij\rangle\sigma} (c_{i\sigma}^\dagger c_{j\sigma} + \text{H.c.}) + U \sum_{i\sigma} \langle n_{i\bar\sigma}\rangle n_{i\sigma}, \quad (10)$$

where $\langle n_{i\sigma}\rangle$ is the expectation value of the number of electron with spin σ at the ith site. In our calculations, we use the open boundary condition and examine finite lattices with $N = 180\,329$ and $1\,049\,137$, where the largest domains are D_6 and D_7, respectively. The lattices are generated by the
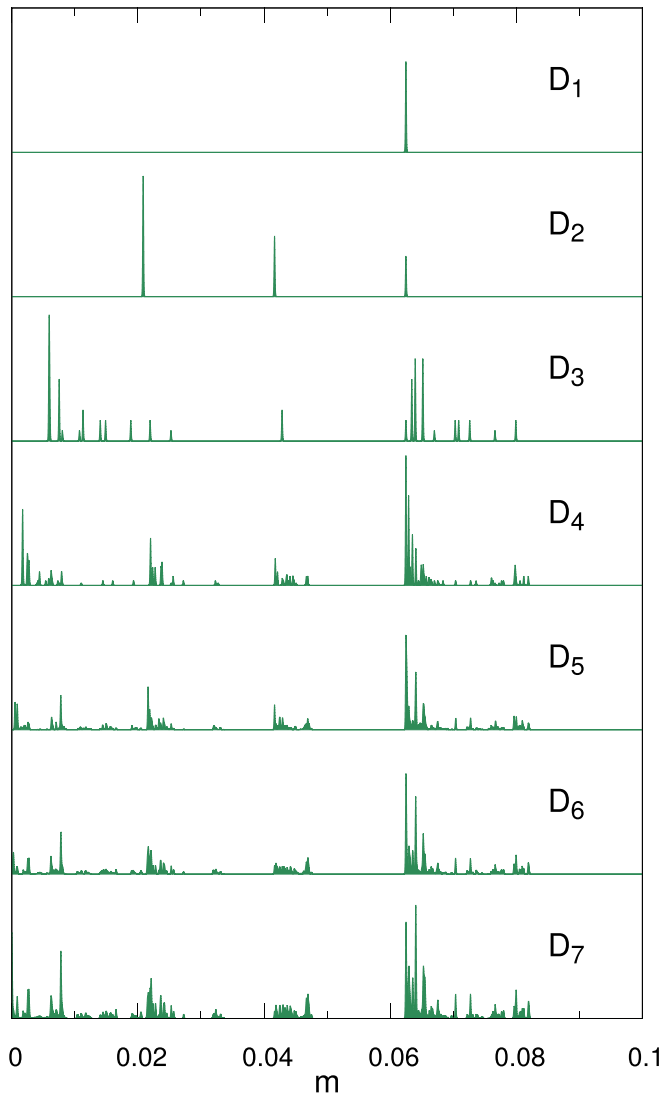
FIG. 9. Local magnetizations in each domain for the Hubbard model on the Ammann-Beenker tiling in the limit $U \to 0$.

deflation operations to the D_1 domain [shown in Fig. 4(a)] and therefore have the global eightfold rotational symmetry. For given values of mean fields, we numerically diagonalize the mean-field Hamiltonian H_{MF} and update the mean fields, and iterate this self-consistent procedure until the result converges within numerical accuracy.

We show in Fig. 10 the spatial pattern of the magnetization $m_i(=\langle n_{i\uparrow} \rangle - \langle n_{i\downarrow} \rangle)/2$ when $U/t = 1.0 \times 10^{-7}$. It is found that finite staggered magnetizations are induced even in the limit. This is due to the existence of the confined states, as discussed above. We note that the F vertices are also magnetized except for the F vertex at the center of the system. This originates from the fact that the amplitude of the confined states at the F_n vertex is zero in the D_n domain, while it should be finite in the larger domains, as discussed before. Therefore, it is naively expected that, in the thermodynamic limit, each lattice site has a finite magnetization even in the weak coupling limit. This is in contrast to the systems with delta-function peak in DOS such as the Lieb and Penrose lattices, where there exist a finite density of nonmagnetic sites. A remarkable point is

that eight A and B vertices around the F vertex have large magnetizations with $m \sim 1/16$ and the other A and B vertices are less magnetized, as shown in Fig. 10. Then, the Ammann-Beenker tiling with the larger lattice constant τ^2 is formed in the spatial distribution of the magnetizations if the F vertex and adjacent A and B vertices with large magnetizations are regarded as its "unit cell." This may imply the superlattice structure (fractal behavior) in the magnetic profile, which will be discussed later.

Increasing the Coulomb interactions, the magnetizations monotonically increase and finally the system should be described by the Heisenberg model in the strong coupling limit. To clarify the crossover in the ordered state between weak and strong coupling regimes, we show in Fig. 11 the distribution of local magnetizations in the system with $N = 180\,329$. When $U/t \to 0$, a finite distribution appears in the magnetization, where the average of the staggered magnetization $\bar{m}_0 \sim 0.043$. This originates from the existence of the macroscopically degenerate states discussed above and the staggered magnetization should be given as $1/4\tau^2$ in the thermodynamic limit. The increase of the Coulomb interactions monotonically increases the absolute value of local magnetization $\bar{m}_i \sim \bar{m}_{i0} + c_i U$, where $\bar{m}_{i0}$ is the local magnetization at $U \to 0$ and c_i is the constant. This U dependence differs from that in the conventional bipartite system, where the staggered magnetization usually increases as $m \sim \exp(-a/U)$, where a is constant. On the other hand, this behavior is common to that in the bipartite systems with the macroscopically degenerate states at the Fermi level such as the Lieb [40] and Penrose [12] lattices. Increasing the interaction strength, the distribution of local magnetizations gradually changes. At last, when $U/t \gtrsim 2$, the magnetizations are classified by some peaks. This classification is closely related to the coordination number for each site, which is different from the weak coupling case. Therefore, the crossover occurs in the antiferromagnetically ordered state around $U/t \sim 1.5$. Namely, in the strong coupling regime, the larger magnetization appears in the A vertices with smaller coordinations. This should be consistent with the QMC results in the strong coupling limit [36,37], where the Hubbard model is reduced to the Heisenberg model, although in the mean-field treatment, quantum fluctuations originating from intersite correlations are underestimated.

Finally, let us study the spatial profile of the magnetizations characteristic of the Ammann-Beenker tiling. To this end, we map it to the perpendicular space. The positions in the perpendicular space have one-to-one correspondence with the position in the physical space. Each vertex site in the Ammann-Beenker tiling is described by the four-dimensional lattice points $\vec{n} = (n_0, n_1, n_2, n_3)$ labeled with integers n_m (see Fig. 1). Their coordinates are the projections onto the two-dimensional space:

$$\mathbf{r} = (x, y) = (\vec{n} \cdot \vec{e}^x, \vec{n} \cdot \vec{e}^y), \tag{11}$$

where $e_m^x = \cos(m\pi/4)$ and $e_m^y = \sin(m\pi/4)$. The projection onto the two-dimensional perpendicular space has information specifying the local environment of each site,

$$\tilde{\mathbf{r}} = (\tilde{x}, \tilde{y}) = (\vec{n} \cdot \tilde{\vec{e}}^x, \vec{n} \cdot \tilde{\vec{e}}^y), \tag{12}$$
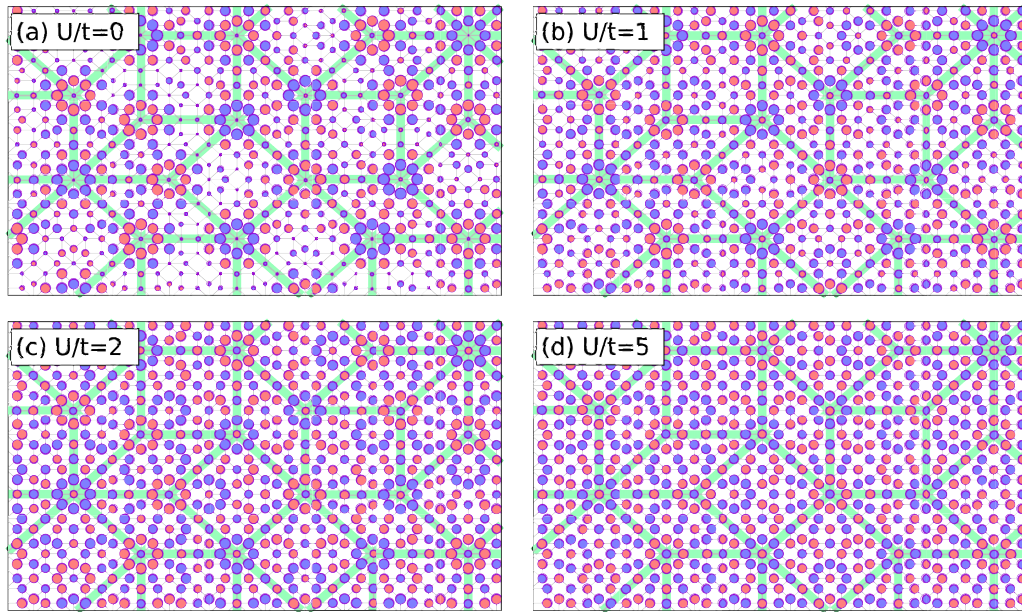
FIG. 10. Spatial pattern for the staggered magnetization in the Hubbard model on the Ammann-Beenker tiling when $U/t = 1.0 \times 10^{-7}$ (essentially the same as $U = 0$), 1, 2, and 5. The area of the circles represents the normalized magnitude of the local magnetization. Bold lines represent the Ammann-Beenker tiling with the lattice constant τ^2.

where $\tilde{e}_m^x = \cos(3m\pi/4)$ and $\tilde{e}_m^y = \sin(3m\pi/4)$. Namely, six kinds of vertices have the corresponding regions in the perpendicular space, as shown in Fig. 12(d). Since vertices in both sublattices are uniformly distributed in the corresponding regions of the perpendicular space, the absolute value of magnetization is shown in Fig. 12. In the weak coupling limit, we find the detailed structure in the perpendicular space, meaning that the magnetization is not classified by the kinds of vertices. Therefore, this magnetic profile is reflected by the spatial structure of the macroscopically degenerate confined states, where large magnetizations appear in the A and B vertices around the F vertices, as shown in Fig. 12(a). Increasing the Coulomb interactions, interesting detailed structures smear in the perpendicular space. When $U/t = 5$, the magnetizations are almost specified by the vertices, where large magnetization appears in the A vertices and small magnetization appears

FIG. 11. Distribution of local magnetizations as a function of the Coulomb interaction U/t in the system with $N = 180\,329$. Dotted lines represent the sublattice average $\bar{m}$.

in the F vertices. This tendency should be consistent with the results obtained from the quantum Monte Carlo simulations [36], as mentioned above.

Before summary, we wish to comment on fractal behavior in the magnetic properties in the weak coupling case. In the spatial distribution, A and B vertices around the F vertex have large magnetizations and these units form the Ammann-Beenker tiling with the lattice constant τ^2, as shown in Fig. 10. This superlattice structure in the magnetizations allows us to consider the perpendicular space for the F vertex lattice. Figure 13(a) shows the magnetization profile for the F vertices in the weak coupling limit, which is the same as that of the F vertex part in Fig. 12(a). The average of the staggered magnetizations for the F vertices $\bar{m}_0^F \sim 0.005$ is much smaller than its bulk average $\bar{m}_0 \sim 0.043$, and therefore the magnetic profile for the F vertices may be invisible in Fig. 12(a). Figure 13(a) clearly shows that the magnetizations are not classified by the kinds of F vertices (F_n), which are octagonally distributed in the perpendicular space, as shown in Fig. 13(b). Instead, we find the detailed structure in the distribution, where "A" and "B" vertices around "F" vertex have large magnetization in the Ammann-Beenker tiling with the lattice constant τ^2. This is similar to that in the original lattice shown in Fig. 12(a). Therefore, we can say that a similar magnetic profile is found in this scale. This may expect a further nested structure in the perpendicular space. Considering the F_i ($i \geqslant 3$) vertex lattice in the Ammann-Beenker tiling with the lattice constant τ^4, we show the magnetic profile in their perpendicular space in Fig. 13(c). We find a similar detailed structure in the staggered magnetizations although the number of the corresponding vertices are not large enough and the absolute value of the magnetization is much smaller. Then, we can say that fractal behavior appears in the magnetization profile, in particular, in the weak coupling limit.
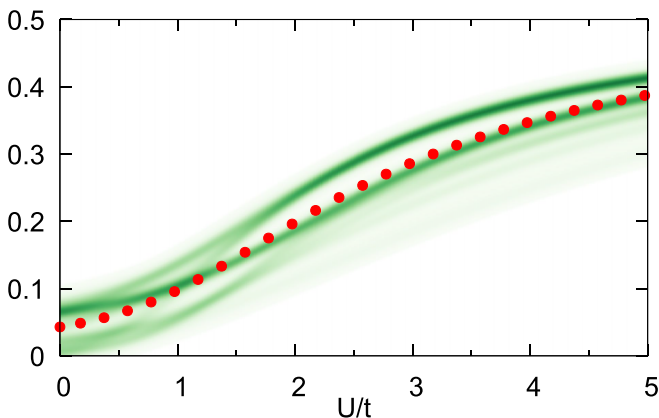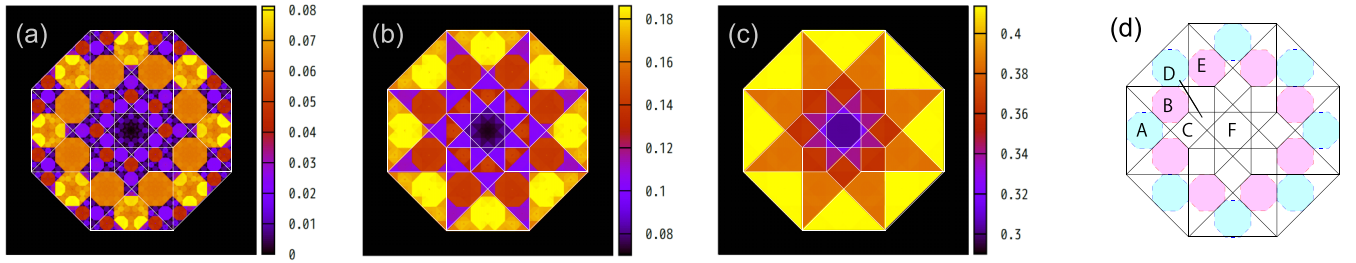
FIG. 12. Magnetization profile in the perpendicular space $(\tilde{x}, \tilde{y})$ for the Hubbard model when (a) $(U/t, N) = (1.0 \times 10^{-7}, 1\,049\,137)$, (b) $(1.5, 180\,329)$, and (c) $(5.0, 180\,329)$. (d) Each area bounded by the solid lines is the region of one of the six types of vertices shown in Fig. 1. Shaded areas bounded by the dashed lines represent the regions of certain A and B vertices, which are the nearest-neighbor and next-nearest-neighbor sites for the F vertices, respectively.

V. SUMMARY

We have investigated magnetic properties in the half-filled Hubbard model on the Ammann-Beenker tiling. Considering the domain structure with locally eightfold rotational symmetry, we have examined the strictly localized confined states. We have then obtained their exact fractions in the thermodynamic limit. In contrast to the vertex model on the Penrose tiling, the wave functions for confined states are densely distributed in the lattice and thereby the introduction of the Coulomb interactions should induce finite staggered magnetizations in each site. Increasing the interaction strength, the spatial distribution of the magnetizations continuously changes to those of the Heisenberg model. Mapping the magnetization profiles to the perpendicular space, we have clarified that the superlattice structure appears in the magnetization profiles. In the realistic quasiperiodic systems realized by the microwave resonators [42] and ultracold atoms [43,44], the hopping integral and/or longer range interactions along the diagonal of the rhombuses with the shortest distance should play an important role in low temperature properties. These interesting problems are now under consideration.

APPENDIX A

Here, we prove that the number of the α vertex is independent of the spin. In the main text, we have proved that the numbers of squares and rhombuses are independent of the spin, $S_\sigma = S/2$ and $R_\sigma = R/2$. Now, we consider the inflation-deflation process for the vertices [31,32]. Each vertex with the spin σ is transformed under the inflation process as

$$
\begin{aligned}
A_\sigma &\to 0 & E_\sigma &\to C_{1\sigma} \\
B_\sigma &\to 0 \\
C_{1\sigma} &\to 0 & F_\sigma &\to \begin{cases} C_{2\sigma} \\ D_\sigma \\ E_\sigma \\ F_\sigma \end{cases}, \quad \text{(A1)} \\
C_{2\sigma} &\to A_\sigma \\
D_\sigma &\to B_\sigma
\end{aligned}
$$

where 0 means that the vertices vanish under the inflation process. Since there are two kinds of the C vertices in the tiling, we have introduced C_1 and C_2 vertices. Under the deflation process, a $C_{1\sigma}$ vertex is not changed from any vertex but is generated inside of each square with spin $\bar{\sigma}$, $S_{\bar{\sigma}}$, as shown in Fig. 2. Therefore $p^{C_{1\sigma}} = p^{S_{\bar{\sigma}}}/\tau^2 = 1/2\tau^3$, where the fraction of the squares with spin σ is $p^{S_\sigma} = S_\sigma / \sum_{\sigma'}(S_{\sigma'} + R_{\sigma'}) = 1/2\tau$. Another $C_{2\sigma}$ vertex is always generated from the A_σ vertex, $p^{C_{2\sigma}} = p^{A_\sigma}/\tau^2$. Note that C_1 and C_2 vertices always appear as the nearest-neighbor pair in the tiling, as shown in Fig. 4. Therefore, we can say that the C_2 vertex is also independent of spin. Since the $C_{2\sigma}$ vertex is always changed to the A_σ (E_σ) vertex under the inflation (deflation) process, $p^{A_\sigma} = p^A/2$ ($p^{E_\sigma} = p^E/2$). Two B_σ vertices are generated inside of each square S_σ and each rhombus R_σ, as shown in
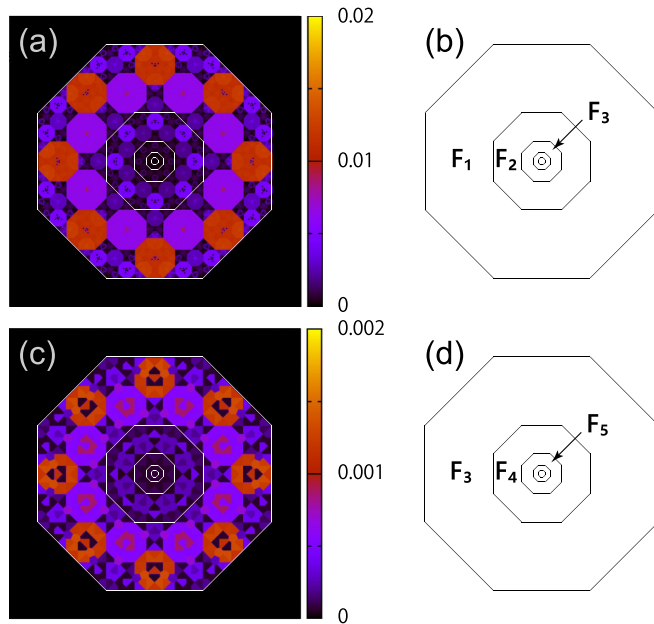

FIG. 13. Magnetization profile in the perpendicular space for the system with $N = 1\,049\,137$ when $U/t = 1.0 \times 10^{-7}$ (essentially same as 0). The results for the F [F_i ($i \geqslant 3$)] vertices are shown in (a) [(c)], and (b) [(d)] each part is the region of F_i vertices.
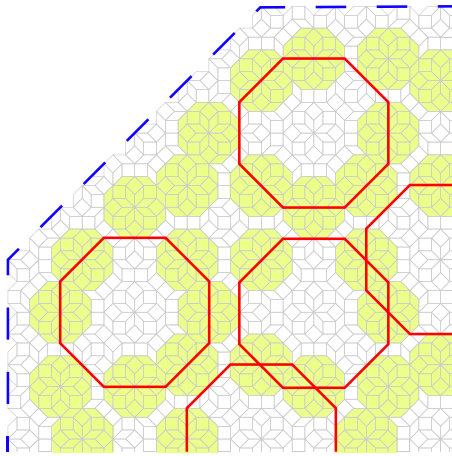
FIG. 14. Quarter of the domain D_4. Shaded regions represent the D_1 domains and octagon regions bounded by the solid lines represent the D_2 domains.

Fig. 2. This implies that the fraction of the B vertex is independent of the spin, $p^{B_\sigma} = p^B/2$. All B_σ vertices are changed

to the D_σ vertices under the deflation process. Therefore, the D vertex is also independent and immediately we find that the F vertices are also independent. Then, we can say that all vertices are independent of spins. Namely, the F_i vertices are also independent since the $F_{i\sigma}$ vertices are generated from the $F_{i-1,\sigma}$ vertices and the $F_{1\sigma}$ vertices are changed from the $C_{2\sigma}$, D_σ, and E_σ vertices under the deflation process.

APPENDIX B

We clarify how the net number of the confined state for each domain is obtained numerically, by considering the D_4 domain as an example. The quarter of the D_4 domain is schematically shown in Fig. 14. It is clearly found that, in the D_4 domain, there exist 104 D_1 domains and 16 D_2 domains ($N_{41} = 104$, $N_{42} = 16$, and $N_{43} = 0$). The total number of the confined states in the D_4 domain is obtained as $N_4^{\text{tot}} = 324$ by means of the exact diagonalization. Then, we obtain the net confined state for the D_4 domain as

$$N_4^{\text{net}} = N_4^{\text{tot}} - N_{41}N_1^{\text{net}} - N_{42}N_2^{\text{net}} - N_{43}N_3^{\text{net}} = 20. \quad \text{(B1)}$$

[1] D. Shechtman, I. Blech, D. Gratias, and J. W. Cahn, Phys. Rev. Lett. **53**, 1951 (1984).

[2] T. Ishimasa, Y. Tanaka, and S. Kashimoto, Philos. Mag. **91**, 4218 (2011).

[3] K. Deguchi, S. Matsukawa, N. K. Sato, T. Hattori, K. Ishida, H. Takakura, and T. Ishimasa, Nat. Mater. **11**, 1013 (2012).

[4] K. Kamiya, T. Takeuchi, N. Kabeya, N. Wada, T. Ishimasa, A. Ochiai, K. Deguchi, K. Imura, and N. K. Sato, Nat. Commun. **9**, 154 (2018).

[5] S. Watanabe and K. Miyake, J. Phys. Soc. Jpn. **82**, 083704 (2013).

[6] N. Takemori and A. Koga, J. Phys. Soc. Jpn. **84**, 023701 (2015).

[7] S. Takemura, N. Takemori, and A. Koga, Phys. Rev. B **91**, 165114 (2015).

[8] E. C. Andrade, A. Jagannathan, E. Miranda, M. Vojta, and V. Dobrosavljević, Phys. Rev. Lett. **115**, 036403 (2015).

[9] R. Shinzaki, J. Nasu, and A. Koga, J. Phys. Soc. Jpn. **85**, 114706 (2016).

[10] J. Otsuki and H. Kusunose, J. Phys. Soc. Jpn. **85**, 073712 (2016).

[11] S. Sakai, N. Takemori, A. Koga, and R. Arita, Phys. Rev. B **95**, 024509 (2017).

[12] A. Koga and H. Tsunetsugu, Phys. Rev. B **96**, 214402 (2017).

[13] S. Sakai and R. Arita, Phys. Rev. Research **1**, 022002 (2019).

[14] Y. Zhang, Y. Liu, W.-Q. Chen, and F. Yang, arXiv:2002.06485.

[15] R. Tamura, Y. Muro, T. Hiroto, K. Nishimoto, and T. Takabatake, Phys. Rev. B **82**, 220201(R) (2010).

[16] A. Ishikawa, T. Hiroto, K. Tokiwa, T. Fujii, and R. Tamura, Phys. Rev. B **93**, 024416 (2016).

[17] A. Ishikawa, T. Fujii, T. Takeuchi, T. Yamada, Y. Matsushita, and R. Tamura, Phys. Rev. B **98**, 220403(R) (2018).

[18] M. Kohmoto and B. Sutherland, Phys. Rev. B **34**, 3849 (1986).

[19] M. Kohmoto and B. Sutherland, Phys. Rev. Lett. **56**, 2740 (1986).

[20] H. Tsunetsugu, T. Fujiwara, K. Ueda, and T. Tokihiro, J. Phys. Soc. Jpn. **55**, 1420 (1986).

[21] B. Sutherland, Phys. Rev. B **34**, 3904 (1986).

[22] T. Hatakeyama and H. Kamimura, Solid State Commun. **62**, 79 (1987).

[23] M. Arai, T. Tokihiro, T. Fujiwara, and M. Kohmoto, Phys. Rev. B **38**, 1621 (1988).

[24] N. Macé, A. Jagannathan, P. Kalugin, R. Mosseri, and F. Piéchon, Phys. Rev. B **96**, 045138 (2017).

[25] S. M. Bhattacharjee, J.-S. Ho, and J. A. Y. Johnson, J. Phys. A **20**, 4439 (1987).

[26] Y. Okabe and K. Niizeki, J. Phys. Soc. Jpn. **57**, 1536 (1988).

[27] J. Oitmaa, M. Aydin, and M. J. Johnson, J. Phys. A **23**, 4537 (1990).

[28] E. S. Sørensen, M. V. Jarić, and M. Ronchetti, Phys. Rev. B **44**, 9271 (1991).

[29] A. Jagannathan, A. Szallas, S. Wessel, and M. Duneau, Phys. Rev. B **75**, 212407 (2007).

[30] K. Inayoshi, Y. Murakami, and A. Koga, J. Phys. Soc. Jpn. **89**, 064002 (2020).

[31] J. E. S. Socolar, Phys. Rev. B **39**, 10519 (1989).

[32] M. Baake and D. Joseph, Phys. Rev. B **42**, 8091 (1990).

[33] R. N. Araújo and E. C. Andrade, Phys. Rev. B **100**, 014510 (2019).

[34] D. Varjas, A. Lau, K. Pöyhönen, A. R. Akhmerov, D. I. Pikulin, and I. C. Fulga, Phys. Rev. Lett. **123**, 196401 (2019).

[35] A. Jagannathan and H. J. Schulz, Phys. Rev. B **55**, 8045 (1997).

[36] S. Wessel, A. Jagannathan, and S. Haas, Phys. Rev. Lett. **90**, 177205 (2003).

[37] A. Jagannathan, Phys. Rev. B **71**, 115101 (2005).

[38] N. Hartman, W.-T. Chiu, and R. T. Scalettar, Phys. Rev. B **93**, 235143 (2016).

[39] E. H. Lieb, Phys. Rev. Lett. **62**, 1201 (1989).

[40] K. Noda, A. Koga, N. Kawakami, and T. Pruschke, Phys. Rev. A **80**, 063622 (2009).

[41] We note that the representations of the confined states are not unique since they are degenerate at $E = 0$ and their linear combination is also a zero energy state. In our paper, we have chosen each confined state so that it is described by the one-dimensional representation of the dihedral group D_8. On the other hand, it may be possible to choose the confined states so that their amplitudes are given only by ± 1. For example, the confined states in the domain D_2 should be defined as $\Psi_{a\pm} = (\Psi_3 \pm \Psi_4)/2$ and $\Psi_{b\pm} = (\Psi_5 \pm \Psi_6)/2$. We have also confirmed that the confined states in the D_3 domain are described by ± 1. However, it is not clear that the confined states in the D_i domains with $i \geqslant 4$ are described in terms of ± 1. It is one of the interesting problems in the Ammann-Beenker tiling, which will be for future work .

[42] P. Vignolo, M. Bellec, J. Böhm, A. Camara, J.-M. Gambaudo, U. Kuhl, and F. Mortessagne, Phys. Rev. B **93**, 075141 (2016).

[43] L. Guidoni, C. Triché, P. Verkerk, and G. Grynberg, Phys. Rev. Lett. **79**, 3363 (1997).

[44] K. Viebahn, M. Sbroscia, E. Carter, J.-C. Yu, and U. Schneider, Phys. Rev. Lett. **122**, 110404 (2019).